



# Outlining the beneficial photocatalytic effect of ZnS deposition in simplistically developed iron oxide nanocomposites of different stoichiometry

Muhammad Muteeb Butt<sup>1</sup> · Talha Farooq Khan<sup>1</sup> · Mohsin Muhyuddin<sup>1</sup> · M. Aftab Akram<sup>2</sup> · Muhammad Zaka Ansar<sup>3</sup> · Muhammad Abdul Basit<sup>1,4</sup> · Sajid Butt<sup>1</sup>

Received: 19 October 2020 / Accepted: 27 February 2021 / Published online: 15 March 2021  
© The Author(s), under exclusive licence to Springer-Verlag GmbH, DE part of Springer Nature 2021

## Abstract

Iron oxide nanoparticles (IONPs) are promising semiconductor photocatalysts driven under visible light owing to their lower bandgap value compared with other metal-oxide nanoparticles (NPs). Owing to the lower cost, IONPs have been combined with other NPs purposefully. In this study, ZnS was deposited on the three most common types of IONPs i.e., magnetite ( $\text{Fe}_3\text{O}_4$ ), hematite ( $\alpha\text{-Fe}_2\text{O}_3$ ) and Goethite ( $\alpha\text{-FeOOH}$ ), targeting improvement in their photocatalytic response. Using a simplistic wet-chemical approach i.e., pseudo-successive ionic layer adsorption and reaction (i.e., *p*-SILAR), resultant  $\text{Fe}_3\text{O}_4/\text{ZnS}$ ,  $\alpha\text{-FeOOH}/\text{ZnS}$ , and  $\alpha\text{-Fe}_2\text{O}_3/\text{ZnS}$  nanocomposites were developed those exhibited higher photocatalytic efficiencies compared to corresponding IONPs. Rhodamine B (RhB) dye was used as a reference for comparative investigation of IONPs without and with ZnS deposition, which revealed that all IONPs were benefited with ZnS deposition, however,  $\text{Fe}_3\text{O}_4$  responded the most by resulting ~3 times higher increase (from 19.3 to 66.5%) in the photocatalytic degradation of RhB. The final order of efficiency for nanocomposites remained as  $\text{Fe}_3\text{O}_4/\text{ZnS} > \alpha\text{-FeOOH}/\text{ZnS} > \alpha\text{-Fe}_2\text{O}_3/\text{ZnS}$  nanocomposites. Individual IONPs and their nanocomposites were explored using customary material characterization techniques and their photocatalytic performance was explained in accordance with the qualitative and quantitative statistics using electrochemical impedance spectroscopy (EIS) as well.

**Keywords**  $\text{Fe}_3\text{O}_4$  ·  $\alpha\text{-Fe}_2\text{O}_3$  ·  $\alpha\text{-FeOOH}$  · ZnS · Nanocomposite · Photocatalysts · Semiconductor

## 1 Introduction

In this modern era, remediation and environmental protection are the key challenges faced by scientists in day-to-day life. Scientific development followed by industrial advancement has exhausted global warming, water contamination and development of uncontrolled ground water [1]. This waste water released by innumerable industries (like cosmetic, food, printing, textile, leather, etc.) holds a huge amount of both organic compounds and inorganic compounds which are non-biodegradable and are quite toxic, thereby creating a massive threat to the environment [2]. In 2009 Soloman et al. [3] and Robinson et al. in 2001 [4] have delineated in their studies that there are approximately 10,000 different types of textile dyes having an annual production of  $7 \times 10^5$  metric tons worldwide. According to another study, approximately 20% of these dyes enter directly into the environment mainly water supply [5]. These

✉ Muhammad Abdul Basit  
ab\_saim@hotmail.com; m.abdulbasit@mail.ist.edu.pk

✉ Sajid Butt  
sajid.butt@ist.edu.pk

<sup>1</sup> Department of Materials Science and Engineering, Institute of Space Technology, Islamabad 44000, Pakistan

<sup>2</sup> School of Chemical and Materials Engineering, National University of Sciences and Technology (NUST), Sector H-12, Islamabad 44000, Pakistan

<sup>3</sup> National Center for Physics, Quaid-I-Azam University, Islamabad, Pakistan

<sup>4</sup> Department of Materials Science and Chemical Engineering, Hanyang University, Ansan 15588, Republic of Korea

dyes are quite perilous for all living species, especially for aquatic life.

Numerous physical and chemical treatments have been established to degrade and remove dye molecules from wastewater, which include techniques like chemical coagulation, adsorption, filtration, chlorination, aerobic, photocatalysis and anaerobic biological treatment, etc. [6]. Among all these reported treatments, photocatalytic degradation techniques are the one which has attracted significant attention for the intoxication of pollutants both organic and inorganic [7]. Photocatalytic degradation process is important because of its competency as it completely converts the toxic organic pollutants into less toxic or water and CO<sub>2</sub> and is a low-temperature process, as well [8]. The tunable bandgap, high surface area, appropriate morphology, constancy and reusability of the catalyst used are striking features of the photocatalytic system [9].

Iron oxide nanoparticles (IONPs) being magnetic have vast applications like magnetic biosensing, magnetic resonance imaging and targeted drug delivery [10–13]. IONPs have also gained massive attention as a photocatalyst due to their high efficiency, high photostability, non-toxicity, eco-friendliness and low production cost [14]. Furthermore, the iron oxides are magnetic due to which they can be conveniently removed and separated from the solution upon application of a magnetic field which is another benefit [15]. IONPs have different compositions and crystal structures like wustite (FeO), maghemite ( $\gamma$ -Fe<sub>2</sub>O<sub>3</sub>), hematite ( $\alpha$ -Fe<sub>2</sub>O<sub>3</sub>), magnetite (Fe<sub>3</sub>O<sub>4</sub>) and Goethite ( $\alpha$ -FeOOH). Another reason for drawing attention is that these oxides absorb light in the visible region, which is approximately 45% of the solar spectrum reaching the earth. Despite all these beneficial traits, iron oxides have limited photocatalytic activity owing to the fast recombination of its photogenerated charge carriers and low separation efficiency [16].

Various strategies have been designed to deal with these drawbacks and to improve the photocatalytic efficiency of iron oxides; including doping [17], composite synthesis with another semiconductor material [18] and morphology controlled synthesis [19], as recommended by numerous researchers. Developing semiconductors such that they have different energy levels is considered best for decreasing the recombination rate of photo-induced charge carriers and improving the charge separation [18]. For instance, Zhang et al. synthesized Fe<sub>3</sub>O<sub>4</sub>/TiO<sub>2</sub>/Ag nanocomposite based on three components for photo-degradation of MB dye under ultraviolet–visible (UV–Vis) radiations using facile chemical deposition route [20]. Their results illustrated that the photocatalytic efficiency of synthesized Fe<sub>3</sub>O<sub>4</sub>/TiO<sub>2</sub>/Ag nanocomposites reached 90%, which was much higher as compared to that of pristine Fe<sub>3</sub>O<sub>4</sub> or TiO<sub>2</sub>. Improved photocatalytic efficiency was attributed to synergetic effects of reduced recombination rate and enhanced light absorption.

Similarly, Kang et al. prepared a hierarchical heterostructure of SnO<sub>2</sub>/Fe<sub>2</sub>O<sub>3</sub> having morphology like necklace through chemical vapor deposition technique [21]. This heterostructure efficiently degraded MB dye under visible light owing to hetero-interface which has improved electron/hole separation efficiency. In another study, Zhu et al. synthesized hierarchical heterostructures of  $\alpha$ -FeOOH nanostructures on TiO<sub>2</sub> nanofibers by a facile hydrothermal method. The as-prepared hierarchical heterostructures retain high surface area for dye adsorption, photocatalytic activity in visible light and efficient charge carrier separation [22]. With the evolution of successive ionic layer adsorption and reaction (SILAR) method, it has become pretty easier to combine effectual nanomaterials for improvement in their visible light absorbance [23], or electron–hole transfer and/or stability [24]. Being an efficient passivation layer used in quantum-dot-sensitized solar cells [25], ZnS deposited by SILAR and/or pseudo-SILAR [39] (i.e., *p*-SILAR process which is a customized SILAR process applied on NPs) offers a good control on detrimental charge recombination inside NPs. In this context, there are no reports regarding the secondary deposition of ZnS on various IONPs and their concomitant results based on comparative photocatalytic performance. i.e., Fe<sub>3</sub>O<sub>4</sub>,  $\alpha$ -Fe<sub>2</sub>O<sub>3</sub> and  $\alpha$ -FeOOH.

Herein, we first compared the photocatalytic properties of magnetite (Fe<sub>3</sub>O<sub>4</sub>), hematite ( $\alpha$ -Fe<sub>2</sub>O<sub>3</sub>), and goethite ( $\alpha$ -FeOOH) NPs and then strategically improved their performance by depositing ZnS on them which resulted in increased efficiency for all the heterostructures i.e., Fe<sub>3</sub>O<sub>4</sub>/ZnS,  $\alpha$ -Fe<sub>2</sub>O<sub>3</sub>/ZnS and  $\alpha$ -FeOOH/ZnS. Detailed characterizations were performed to study the photocatalytic properties of as-procured IONPs and the synthesized nanocomposites using Rhodamine B (RhB) dye as the targeted pollutant. It was found that Fe<sub>3</sub>O<sub>4</sub>/ZnS nanocomposite showed 66.4%,  $\alpha$ -Fe<sub>2</sub>O<sub>3</sub>/ZnS nanocomposite showed 52.2% and  $\alpha$ -FeOOH/ZnS nanocomposite showed 61.4% better performance as compared to the pristine IONPs.

## 2 Experimental

### 2.1 Iron oxide nanoparticles (IONPs)

High purity IONPs having different compositions of Fe<sub>3</sub>O<sub>4</sub>,  $\alpha$ -Fe<sub>2</sub>O<sub>3</sub> and  $\alpha$ -FeOOH were acquired from a local distributor (DS Enterprises, Lahore, Pakistan) of YIPIN Pigments, Germany, having a specification of black oxide (Detech 4330), red oxide (S-130) and yellow oxide S-313, respectively.

## 2.2 Deposition of ZnS

To deposit ZnS over IONPs via *p*-SILAR process [26], we prepared 0.2 M cationic and anionic solution using zinc nitrate and sodium sulfide salts in methanol and deionized (DI) water. 0.1 g of Fe<sub>3</sub>O<sub>4</sub> nanoparticles were taken in centrifuge tubes of 50 ml and 20 ml of Zn<sup>2+</sup> precursor solution was poured in the same centrifuge tube. Stirring was done for 1 min to uniformly disperse particles in the solution and then the obtained mixture was centrifuged at 4000 rpm for 4 min. Upon the completion of centrifuging, the excess liquid was decanted from the tubes in empty beakers. Rinsing was then done with 20 ml methanol and tubes were centrifuged as per the above-given centrifugal conditions to rinse off the loosely attached cations from our base powder. Methanol was then disposed of upon the completion of this step and then 20 ml of S<sup>2-</sup> precursor solution was introduced in the tubes. The tubes were then centrifuged as per previous conditions so that S<sup>2-</sup> ions react with already adsorbed cations on the base powder surface and as a result of this reaction we get a layer of ZnS on the surface of Fe<sub>3</sub>O<sub>4</sub>. After the completion of centrifuging, the solution was decanted in a beaker, and again washing was done with methanol. As the cycle completes with this step, eight cycles were repeated as reported by Khan et al. [27], they deposited ZnS on ZnO nanoflowers and reported optimal deposition at 08 number of cycles. Since our purpose was to obtain the same deposition and compare the effects of deposition so we used reported cycles from the literature. The same process was then repeated for α-Fe<sub>2</sub>O<sub>3</sub> and α-FeOOH nanoparticles as well to achieve the deposition of ZnS. The whole process of

*p*-SILAR has been summarized in the schematic diagram, as shown in Fig. 1.

## 2.3 Characterization

Morphology and topography of the samples were analyzed using field emission-scanning electron microscope (FE-SEM, MIRA3 TESCAN). Compositional analysis and elemental area mapping were performed using energy-dispersive x-ray spectroscopy (EDX) of Oxford detector, equipped with the same SEM. Particle sizes were determined using a laser diffraction particle size analyzer (MASTER-SIZER Malvern). Phase identification was performed using x-ray diffraction (GNR-EXPLORER) and the functional groups were identified by performing Fourier transform infrared spectroscopy (iS50 FTIR spectrometer, Thermo Scientific). UV-visible spectrophotometer (JENWAY-7315) was used to determine the light-harvesting capability of IONPs and their nanocomposites with ZnS. The electrochemical behaviors of pristine IONPs and synthesized nanocomposites were studied through electrochemical impedance spectroscopy (EIS) on a biologic VSP electrochemical workstation. A three-electrode system having platinum (counter electrode; CE), Ag/AgCl as a reference electrode and a glassy carbon disk of 3 mm diameter as a working electrode in 0.6 M KOH electrolyte solution were used to carry out an electrochemical study as described by Little et al. [28]. The working electrode was prepared by making a homogeneous solution of catalyst in 5 ml of methanol followed by the addition of 10 μl of Nafion (binder) which was then sonicated for 30 min. A glassy carbon electrode was then taken and

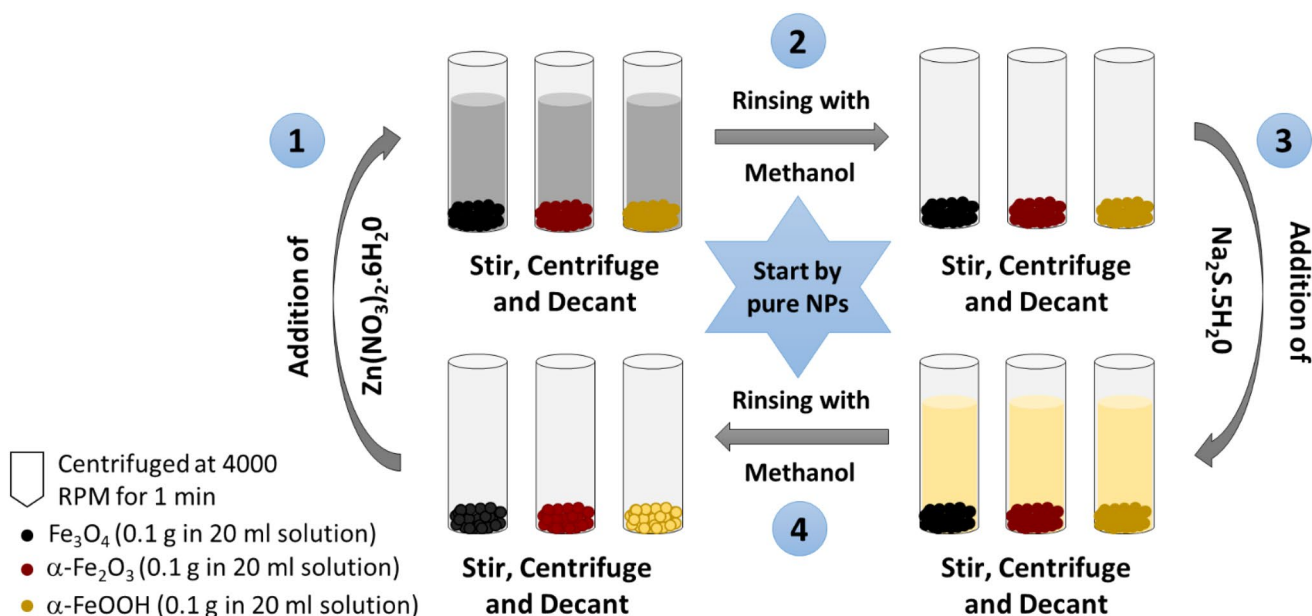


Fig. 1 Schematic diagram for the production of ZnS sensitized iron oxide nanocomposites, showing one cycle of *p*-SILAR process

the prepared mixture was drop casted on it which was then simply dried in an oven.

## 2.4 Evaluating photocatalytic activity

The photocatalytic activity of pristine IONPs and synthesized nanocomposites was determined by degradation of Rhodamine B (RhB) dye under visible light irradiations. Dye solution of 50 ml was taken and 20 mg of each photocatalyst was dispersed into it [29] and the pH value of solution was maintained at 4. A magnetic stirrer was used for the efficient mixing of solutions for around 10 min under dark conditions. Then we exposed our suspensions to visible light using a Xenon arc lamp coupled with a UV cut-off filter. We took 4 ml of the sample after a regular interval of 10 min to 100 min each to analyze the reaction process by determining the light absorption of all samples by using a UV–visible spectrophotometer. Finally, the dye degradation rate was calculated using the following expression;

$$\text{Degradation Rate (\%)} = \left(1 - \frac{C_t}{C_o}\right) \times 100 \quad (1)$$

whereas  $C_o$  refers to initial and  $C_t$  refers to the concentrations of dye at time “ $t$ ”.

## 3 Results and discussion

FE-SEM analysis was performed to study the morphological features of IONPs before deposition of ZnS. Micrographs as illustrated in Fig. 2a–c clearly show that  $\text{Fe}_3\text{O}_4$  and  $\alpha\text{-Fe}_2\text{O}_3$  possess nearly spherical shapes [30] with trivial agglomeration, while,  $\alpha\text{-FeOOH}$  possess rod like morphology [31]. Particle size analysis was also performed and results are shown in Fig. 2d–e. It was found that for  $\text{Fe}_3\text{O}_4$  and  $\alpha\text{-Fe}_2\text{O}_3$  more than 50% of particles showed sizes below 100 nm and the size above nanometer range was associated with the agglomeration as shown in SEM images. For  $\alpha\text{-FeOOH}$  the size varied from 20 to 400 nm as shown in Fig. 2f, the variation in size was attributed to its rod-like shape [31], which might have given different size values with respect to its orientation, which may have created spread in the graph. Elemental composition of the purchased nanoparticles was analyzed in EDS, which showed peaks of only Fe and O establishing the absence of impurities as shown in Fig. S1. During FE-SEM analysis of synthesized nanocomposites, no significant difference was observed in the morphology and size of synthesized nanocomposites after the deposition as shown in Fig. S2(a–c). This may be due to the smaller size or quantity of ZnS that is difficult to characterize and scan through FE-SEM. Similar depositions of metal chalcogenides have been revealed using transmission electron

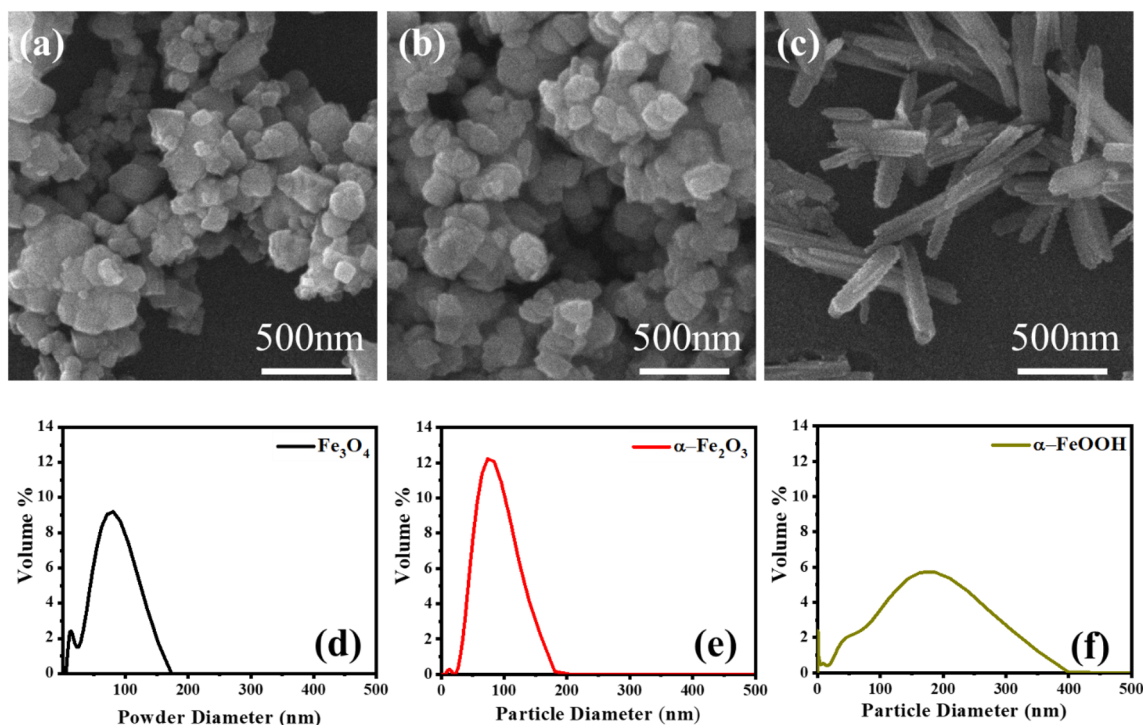
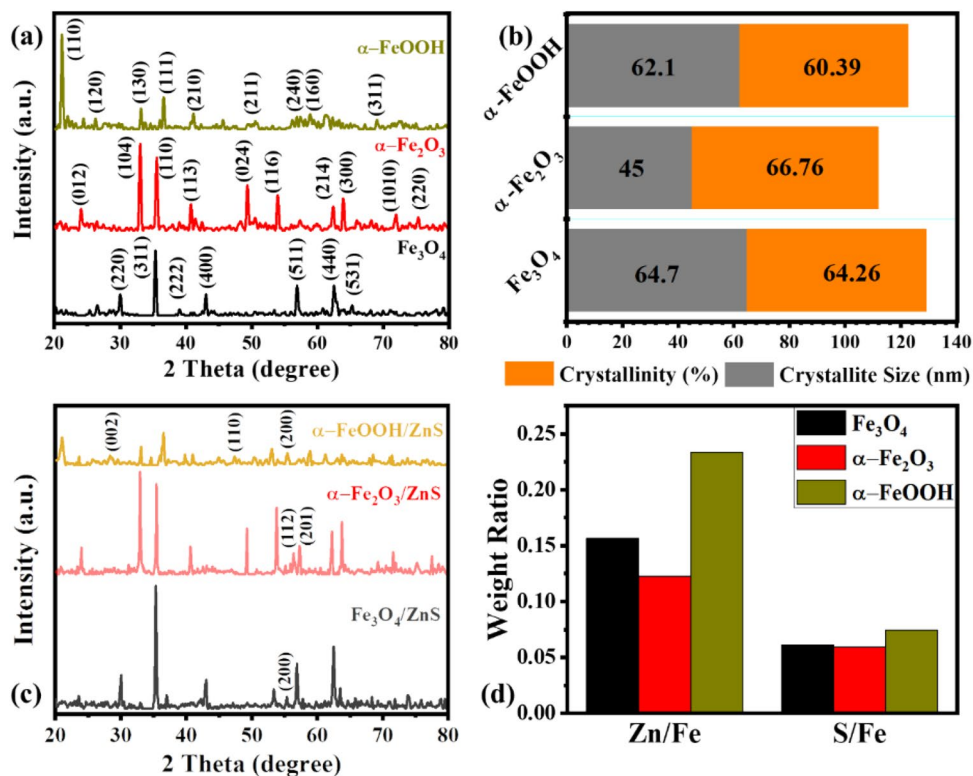


**Fig. 2** FESEM images and particle size analysis of purchased **a, d**  $\text{Fe}_3\text{O}_4$ , **b, e**  $\alpha\text{-Fe}_2\text{O}_3$  and **c, f**  $\alpha\text{-FeOOH}$  nanoparticles, at 100k $\times$  magnification.

microscopy by Khan et al. (i.e., CdS over ZnO nanostructures) [26] and Abbas et al. (i.e., PbS QDs on macroporous TiO<sub>2</sub>) [32], however, other authors have occasionally represented the similar low-scale deposition of metal sulfides [27] using SEM–EDS-based elemental area mapping. Although it is not equally effectual, but good enough to have a comparative elucidation of depositions and their contrasting role for photoactivities, etc. However, uniform deposition of ZnS over the entire surface of all three iron oxides was confirmed EDS mapping, as shown in Fig. S2(d–f) where the Fe, O, Zn and S elements were homogeneously dispersed over the complete profile, affirming successful deposition of ZnS. Deposition of ZnS over IONPs was further confirmed by performing EDS, results in Fig. S3 showed peaks of Zn and S along with Fe and O confirming the deposition of ZnS [27]. XRD patterns of Fe<sub>3</sub>O<sub>4</sub>, α-Fe<sub>2</sub>O<sub>3</sub> and α-FeOOH nanoparticles shown in Fig. 3a and the peaks obtained were in good agreement with those of standard cards; magnetite pattern (JCPDS: 89-0691) [33], α-Fe<sub>2</sub>O<sub>3</sub> pattern (JCPDS card number 33–0664) [34] and goethite pattern (JCPDS card number 29-0713) [35]. Furthermore, the absence of any other strong peak corroborated the purity level of these IONPs. Debye–Scherrer equation [36] was used to estimate the average crystallite size of Fe<sub>3</sub>O<sub>4</sub>, α-Fe<sub>2</sub>O<sub>3</sub> and α-FeOOH nanoparticles which were found to be 64.7 nm, 45 nm and 62.1 nm, respectively. Percentage crystallinity was found to be 64.26%, 66.76% and 60.39% for Fe<sub>3</sub>O<sub>4</sub>, α-Fe<sub>2</sub>O<sub>3</sub> and α-FeOOH nanoparticles, respectively, as shown in Fig. 3b.

XRD analysis of Fe<sub>3</sub>O<sub>4</sub>/ZnS nanocomposite showed an additional peak at 55.3° corresponding to the plane (200) of ZnS, α-Fe<sub>2</sub>O<sub>3</sub>/ZnS nanocomposite showed additional peaks at 56.5° and 57.4° corresponding to the plane (112) and (201) of ZnS and α-FeOOH/ZnS nanocomposite showed additional peaks at 28.3°, 47.3° and 55.3° corresponding to the plane (002), (110) and (200) of ZnS (JCPDS number 79-2204). The XRD results confirm the successful deposition of ZnS as shown in Fig. 3c. Weight ratios of Zn/Fe and S/Fe were calculated for all three nanocomposites using values obtained through EDS analysis as shown in Fig. 3d, so that the relative deposition is accessed. Moiz et al. [26] have recently established that despite similar deposition conditions, the morphology of NPs significantly affects the amount of deposition of CdS on ZnO by p-SILAR. Therefore, it is quite as per expectation that Zn/Fe and S/Fe value was maximum for α-FeOOH which had rod like structure, the reason for this trend was attributed to its shape as it may have maximum surface area or it may have crystallographic planes favorable for deposition or are relatively more active. It could have been much more revealing to compare the transmission electron microscopic contrast however covering the major scope of the issue we added results for optimal α-Fe<sub>2</sub>O<sub>3</sub>/ZnS here (Fig. S4). A well spread network of ZnS particles over the base Fe<sub>2</sub>O<sub>3</sub> was observed that was credited to the presence of tiny ZnS particles throughout the matrix [24] and was equally indicated by the EDS-based area mapping of α-Fe<sub>2</sub>O<sub>3</sub>/ZnS. Moreover, about 0.33 nm distant

**Fig. 3** a XRD patterns of IONPs, b crystallite size and percentage crystallinity of IONPs, c XRD patterns after deposition of ZnS on IONPs, d weight ratio Zn/Fe and S/Fe in Fe<sub>3</sub>O<sub>4</sub>, α-Fe<sub>2</sub>O<sub>3</sub> and α-FeOOH based ZnS nanocomposites measured by EDS



lattice fringes were also detected referring to the presence of (100) plane of ZnS.

FTIR analysis was performed to identify the functional group as well as chemical bonds in IONPs, and to confirm the deposition of ZnS. Pure  $\text{Fe}_3\text{O}_4$  as shown in Fig. 4a gave a peak at  $640\text{ cm}^{-1}$  which is ascribed to the stretching vibrations associated with Fe–O bonds in the crystalline structure of  $\text{Fe}_3\text{O}_4$  [37]. Pure  $\alpha\text{-Fe}_2\text{O}_3$  as shown in Fig. 4b showed a broad band starting from  $3410\text{ cm}^{-1}$  which is due to the stretching vibration of  $\text{OH}^-$  group, while absorption peak at  $640\text{ cm}^{-1}$  corresponds to Fe–O band vibration [37]. Pure  $\alpha\text{-FeOOH}$  as shown in Fig. 4c showed an absorption band at  $3110\text{ cm}^{-1}$  which is ascribed to stretching vibration of a hydroxyl group, the other two sharp peaks were obtained at  $895\text{ cm}^{-1}$  and  $797\text{ cm}^{-1}$  which is attributed to bending vibration of Fe–O–H, while the band at  $640\text{ cm}^{-1}$  is associated with the stretching vibration of Fe–O bond in the material [31]. FTIR of all three synthesized nanocomposites showed an additional peak at  $1004\text{ cm}^{-1}$  which is associated with Zn–S bond vibration [38].

Optical absorption spectra obtained for  $\text{Fe}_3\text{O}_4$ ,  $\alpha\text{-Fe}_2\text{O}_3$ ,  $\alpha\text{-FeOOH}$  and  $\text{Fe}_3\text{O}_4\text{-ZnS}$ ,  $\alpha\text{-Fe}_2\text{O}_3\text{-ZnS}$ ,  $\alpha\text{-FeOOH-ZnS}$  are shown in Fig. 4d–f. Absorbance curves for all pure iron oxides showed intense absorption between 400–700 nm region. Initially, it was observed that all the iron oxides showed a decreasing trend of absorption in the UV range i.e., for wavelength less than 400 nm. However, after deposition of ZnS a significant change in the trend was observed, and the developed  $\text{Fe}_3\text{O}_4\text{-ZnS}$ ,  $\alpha\text{-Fe}_2\text{O}_3\text{-ZnS}$ ,  $\alpha\text{-FeOOH-ZnS}$  nanocomposites started to respond in the UV region. It was

observed that instead of decreasing, the value of absorption tends to increase in UV region which is an indication that ZnS has been successfully deposited [39]. An increase in the visible range absorbance was also observed for all three nanocomposites owing to broadening of density of states by incorporation of ZnS thus more number of photons in wider range of wavelengths are absorbed and also due to the high refractive index of ZnS (2.35) due to which it acted as an antireflection coating (ARC) [40]. In the presence of ARC, light will bend into IONPs instead of being reflected away, resulting in an increase in the light absorbance into IONPs and hence the performance [40]. Bandgap ( $E_g$ ) of IONPs was calculated using *Tauc–Mott* plots [41] which are derived from the absorption spectra as shown in Fig. S5.  $E_g$  values were found to be 1.70 eV for  $\text{Fe}_3\text{O}_4$  [42], 1.82 eV for  $\alpha\text{-Fe}_2\text{O}_3$  [43] and 2.45 eV for  $\alpha\text{-FeOOH}$  [41] and in similarity with referred reports.

The increase in absorbance of ZnS deposited IONPs was equally evident from photocatalytic degradation of RhB as shown in Fig. 5. The normalized visible absorbance peaks of IONPs are, respectively, shown (Fig. 5a–c). The spectra showed a main characteristic peak at 553 nm, which was used to study the concentration of RhB dye during degradation process, spectra also showed a shoulder at around 498 nm which was due to the presence of dimer species [44]. After the deposition of ZnS, the UV–Vis absorbance spectra of  $\text{Fe}_3\text{O}_4\text{-ZnS}$  (Fig. 5d),  $\alpha\text{-Fe}_2\text{O}_3\text{-ZnS}$  (Fig. 5e) and  $\alpha\text{-FeOOH-ZnS}$  (Fig. 5f) showed an evident lowering in 100 min of visible light exposure, affirming the faster degradation of RhB molecules. Initially,  $\alpha\text{-Fe}_2\text{O}_3$  stood the best

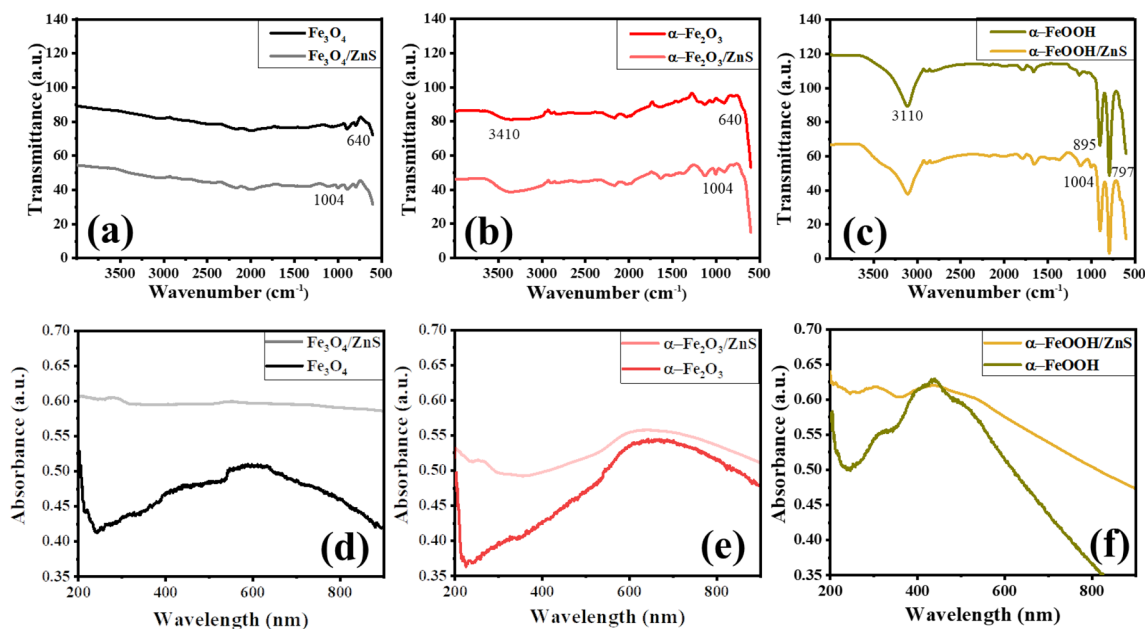


**Fig. 4** FTIR patterns and UV–Vis absorption spectra before and after deposition of ZnS over **a, d**  $\text{Fe}_3\text{O}_4$ , **b, e**  $\alpha\text{-Fe}_2\text{O}_3$  and **c, f**  $\alpha\text{-FeOOH}$  nanoparticles and their nanocomposite

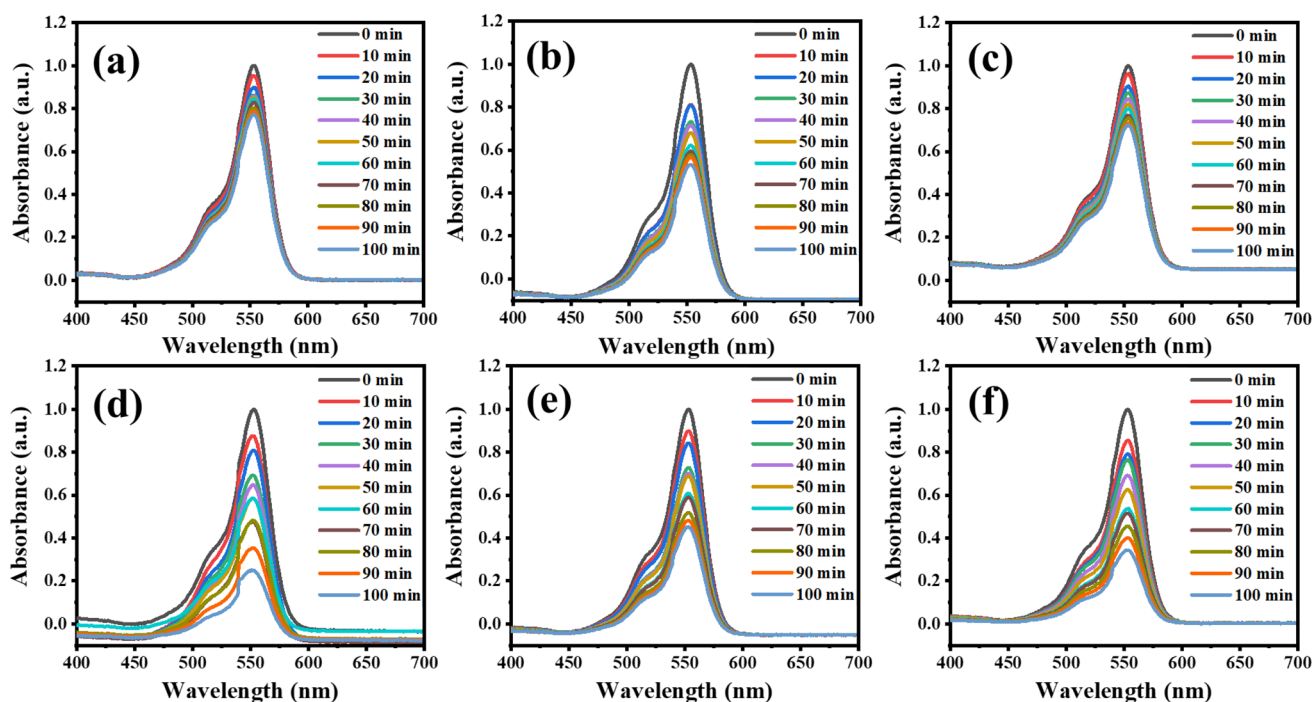


**Fig. 5** UV/Vis spectrum of Rhodamine B dye solution after undergoing different time of visible light irradiation with **a**  $\text{Fe}_3\text{O}_4$ , **b**  $\alpha\text{-Fe}_2\text{O}_3$ , **c**  $\alpha\text{-FeOOH}$ , **d**  $\text{Fe}_3\text{O}_4\text{-ZnS}$ , **e**  $\alpha\text{-Fe}_2\text{O}_3\text{-ZnS}$  and **f**  $\alpha\text{-FeOOH-ZnS}$  nanocomposites

among three IONPs as a photocatalyst which is possibly credited to its lower degree of intrinsic defects because its bandgap as calculated above lie between  $\text{Fe}_3\text{O}_4$  and  $\alpha\text{-FeOOH}$ . However, after the deposition of ZnS,  $\text{Fe}_3\text{O}_4\text{-ZnS}$  attained the optimal credit which reflected its superior response for deposition of ZnS. Figure 6a shows the degradation percentage of RhB dye as a function of irradiation time in the presence of IONPs before and after the deposition of ZnS by *p*-SILAR. Figure 6b shows dye degradation efficiencies of synthesized  $\text{Fe}_3\text{O}_4\text{-ZnS}$ ,  $\alpha\text{-Fe}_2\text{O}_3\text{-ZnS}$  and  $\alpha\text{-FeOOH-ZnS}$  nanocomposites which were 47.17%, 12.34% and 34.20% higher in comparison to respective IONPs. A comparison between the photocatalytic activity of IONPs and synthesized nanocomposites is shown in Fig. 6c. Results showed that the photocatalytic activity of synthesized nanocomposite significantly increased from their respective IONPs due to significant increase in visible light absorption capability of nanocomposites resulting from broadening and increase in density of states in nanocomposites. Since a linear decrease in the tendency of dye with the time of reaction was observed which showed that photocatalytic degradation of RhB dye followed zero-order kinetics [45]. In Fig. S6, the plot between  $C_0 - C$  versus time is shown with values of rate constant. The value of rate constant,  $k$ , for  $\text{Fe}_3\text{O}_4\text{-ZnS}$  nanocomposite is  $5.91 \times 10^{-8} \text{ mol L}^{-1} \text{ min}^{-1}$ , which is about 3.4 times greater than that for  $\text{Fe}_3\text{O}_4$ . For  $\alpha\text{-Fe}_2\text{O}_3\text{-ZnS}$  nanocomposite, the value of  $k$  is  $4.64 \times 10^{-8} \text{ mol L}^{-1} \text{ min}^{-1}$ ,

which is about 1.3 times greater than that for  $\alpha\text{-Fe}_2\text{O}_3$ . For  $\alpha\text{-FeOOH-ZnS}$  nanocomposite, the value of  $k$  is  $5.46 \times 10^{-8} \text{ mol L}^{-1} \text{ min}^{-1}$ , which is about 2.2 times greater than that for  $\alpha\text{-FeOOH}$ . Shi et al. [46] prepared a similar heterostructure by growing CdS on  $\alpha\text{-Fe}_2\text{O}_3$  nanorods and studied its dye degradation properties using Methylene Blue (MB) dye. They reported an increase the performance of  $\alpha\text{-Fe}_2\text{O}_3$  nanorods from 30.6 to 86% after 120 min of irradiation. The enhancement was attributed to the large surface area of nanorods and superior charge transportation. Kang et al. [21] synthesized heterostructure by growing  $\text{SnO}_2$  on  $\alpha\text{-Fe}_2\text{O}_3$  via CVD technique. They used MB dye as a sample pollutant and reported to enhance the performance of  $\alpha\text{-Fe}_2\text{O}_3$  nanoparticles from 58% to approximately 95% after 2.5 h of irradiation time. Despite of the application of various strategies regarding the deposition of secondary materials on one of the IONPs, the corresponding performance remained lower and/or there has been no direct comparison of evaluating the effect of single material such as ZnS on IONPs of different stoichiometry. Keeping in view our experimental results and analysis, the proposed photocatalytic mechanism for all of the synthesized nanocomposites is shown in Fig. 6d. The improvement in the performance may be attributed to two factors: Firstly, it was observed that developed nanocomposites showed relatively higher absorbance in visible range which might have occurred due to the well-known antireflection behavior of ZnS as an over layer

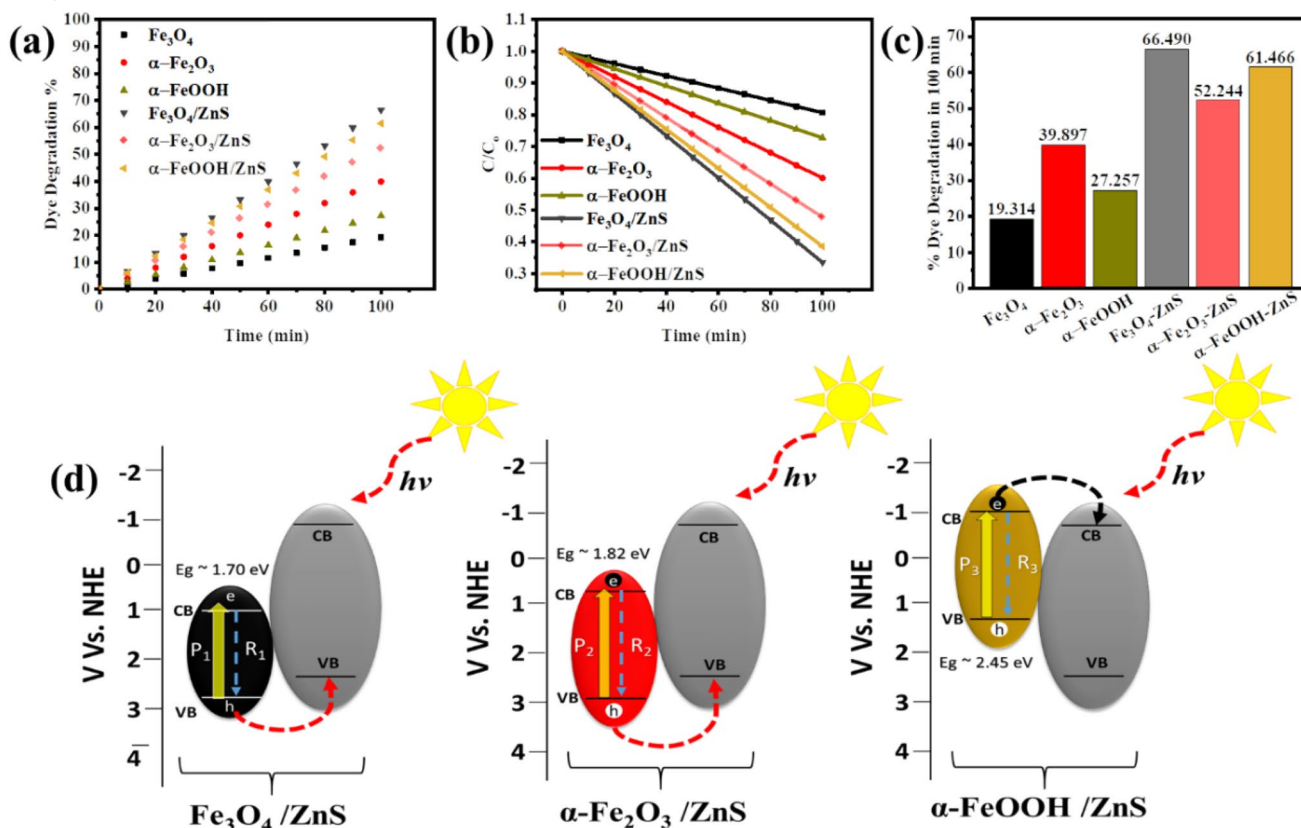


**Fig. 6** **a** Dye degradation percentage under the visible light irradiation **b** extent of photocatalytic degradation **c** dye degradation percentage in 100 min **d** proposed schematic diagram for e–h generation in synthesized nanocomposites

[4, 41] and increased light absorbance. Hence, the developed nanocomposites revealed higher photocatalytic efficiencies because the light was efficiently absorbed. Secondly, for Fe<sub>3</sub>O<sub>4</sub>/ZnS nanocomposite it is known that the conduction band (CB) of ZnS is more negative as compared to the conduction band of Fe<sub>3</sub>O<sub>4</sub> while the valence band (VB) of ZnS was less positive as compared to the valence band of Fe<sub>3</sub>O<sub>4</sub> [47, 48]. This arrangement of bands as represented schematically in Fig. 6d allow interband transition of holes from VB of Fe<sub>3</sub>O<sub>4</sub> nanoparticle to VB of ZnS and hinders the transfer of electron to ZnS, hence expected to reduce the recombination of charge. Due to this charge separation, electrons are available at the oxide surface while holes are present at the sulfide surface and both participate in the degradation of dye. As it was also found that pristine Fe<sub>3</sub>O<sub>4</sub> had the lowest bandgap (1.70 eV) of all three oxides but it showed minimum dye degradation results (19.3%) while after deposition of ZnS it degraded maximum quantity of dye (66.4%). This trend indicated that photo-excitation (P<sub>1</sub>) is maximum in Fe<sub>3</sub>O<sub>4</sub> nanoparticles but due to recombination (R<sub>1</sub>) which is speculated to be maximum in this case, the pristine oxide nanoparticles were not able to degrade the dye. For α-Fe<sub>2</sub>O<sub>3</sub>/ZnS nanocomposite as per available literature, it is also

known that CB of ZnS is generally more negative as compared to the CB of α-Fe<sub>2</sub>O<sub>3</sub> while VB of ZnS is less positive as compared to the VB of α-Fe<sub>2</sub>O<sub>3</sub> [48]. Such an arrangement of bands allows the interband transition of holes from VB of α-Fe<sub>2</sub>O<sub>3</sub> nanoparticle to VB of ZnS and hinder the electron to transfer to ZnS, hence electron at oxide surface and hole present at sulfide surface degrade the dye individually. Bandgap of pure α-Fe<sub>2</sub>O<sub>3</sub> nanoparticle was found to be in between of Fe<sub>3</sub>O<sub>4</sub> and α-FeOOH nanoparticles, despite which it showed maximum dye degradation efficiency and after the deposition of ZnS the increase in efficiency is minimum which indicates that photo-excitation (P<sub>2</sub>) is good and recombination (R<sub>2</sub>) of charge carriers is minimum in this case. For α-FeOOH/ZnS nanocomposite it was found that CB of α-FeOOH is more negative as compared to that of ZnS and the VB of α-FeOOH is less positive as compared to that of ZnS [49]. Such an alignment of bands favors the interband transition of electrons to CB of ZnS while hindering the transfer of holes to VB of ZnS, so in this case, holes will remain at oxide surface and electrons are present at zinc sulfide surface and dye degradation reaction is speculated to occur at both sites/materials. Bandgap of α-FeOOH nanoparticles was found to be maximum (2.45 eV) but it showed



more degradation than  $\text{Fe}_3\text{O}_4$  nanoparticles which had a lower bandgap (1.70 eV). After the deposition of ZnS nanoparticles, the degradation efficiency was improved from 27 to 61% which shows that photo-excitation (P3) was high while recombination (R3) of charge carriers was also high due to which pristine nanoparticles were not able to perform as per their potential, and retrieved their performance after apposite ZnS deposition. The trend in dye degradation performances of  $\alpha\text{-Fe}_2\text{O}_3$ ,  $\text{Fe}_3\text{O}_4$ ,  $\alpha\text{-FeOOH}$  and the nanocomposites (NCs) of aforementioned nanomaterials (NMs) with ZnS, were further supported by analyzing the charge collection dynamics and structural stability against charge recombination through EIS; as reported by Balu et al. [50] and Naeem et al. [51]. The achieved Nyquist's spectra as shown in Fig. 7 were acquired after fitting the equivalent circuit (inset of Fig. 7), comprising of two resistances (R1 and R2) and a capacitor (C). The values of R1, R2 and C are summarized in Table S1. R1 is a non-zero intercept of real-axis and it depicts an overall resistance of the working electrode (i.e., connectors, wires and glassy carbon electrodes, etc.) [52]; therefore, R1 values were almost similar for all the developed materials. Whereas R2 is charge transfer resistance across the catalyst/electrolyte interface and in Nyquist's plots the semi-circle with least diameter shows the smallest value of R2 [52]. It is obvious from the graph that the values of R2 in pure samples were initially in the order of  $\text{Fe}_3\text{O}_4 > \alpha\text{-FeOOH} > \alpha\text{-Fe}_2\text{O}_3$ . However, after deposition of ZnS the lowest R2 was observed for  $\text{Fe}_3\text{O}_4/\text{ZnS}$ , confirming its highest catalytic activity. The deposition of ZnS significantly improved the charge collection efficiencies via fast transportation of charges from the catalyst surface to the dye molecules owing to lower charge transfer resistances (R2). Hence, the strategy of depositing ZnS would be highly beneficial in the reduction of electron-hole recombination rates

by extending the lifetime of charge carriers [50, 51]. Further, to support our results Bode phase plots were employed as shown in Fig. 7b and electron lifetime  $\tau$  was calculated using the Bode phase equation;

$$\tau = \frac{1}{2\pi f_{\text{mid}}} \quad (2)$$

The peak of Bode curves corresponds to the maximum mid frequency, denoted as  $f_{\text{mid}}$  and can be used to calculate electron lifetime [52]. From the plot, it is quite noteworthy that curves shifted towards a lower value of frequency affirming that electron lifetime was increased due to the deposition of ZnS on all three forms of IONPs.

## 4 Conclusion

In summary, we confirmed that the iron oxide-based NPs (IONPs) can significantly be improved in their photocatalytic behavior by simplistic deposition of ZnS via *p*-SILAR. On the one hand, ZnS provides an increase in the visible light absorbance owing to its antireflection nature, while on the other side it lowers down the e-h recombination behavior inside NPs. Resultantly, morphologically different  $\text{Fe}_3\text{O}_4$ ,  $\alpha\text{-Fe}_2\text{O}_3$  and  $\alpha\text{-FeOOH}$  are transformed to superior  $\text{Fe}_3\text{O}_4/\text{ZnS}$ ,  $\alpha\text{-Fe}_2\text{O}_3/\text{ZnS}$  and  $\alpha\text{-FeOOH}/\text{ZnS}$  nanocomposite form. An EIS-based insight affirmed the speculated proficient combination of ZnS with IONPs and signaled towards the productive utility of resultant nanocomposites in terms of optoelectronic use.

**Supplementary Information** The online version contains supplementary material available at <https://doi.org/10.1007/s00339-021-04401-3>.

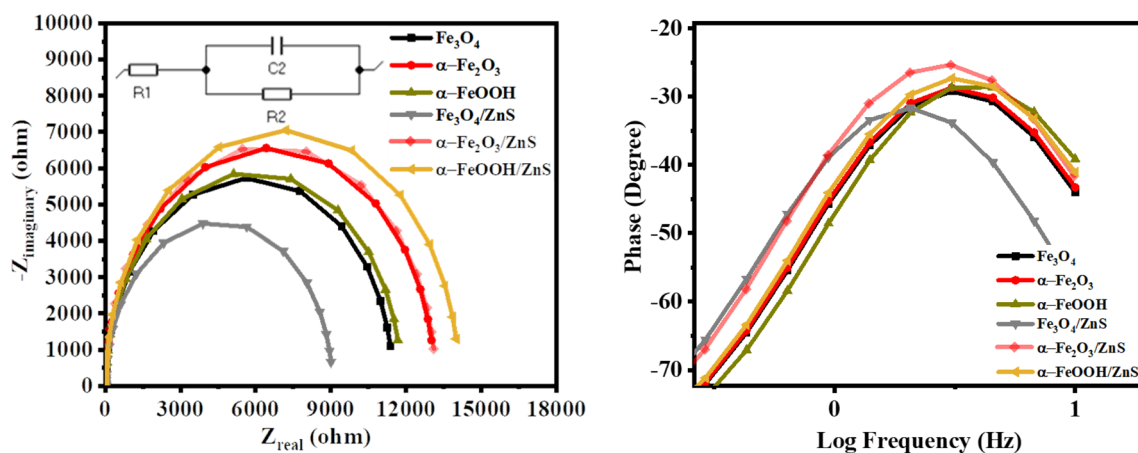


**Fig. 7** a EIS-based Nyquist plots b Bode phase plots for pristine IONPs and resultant nanocomposites synthesized as a result of ZnS deposition by *p*-SILAR

## Declarations

**Conflict of interest** The authors declare that they have no known competing financial interests or personal relationships that could have appeared to influence the work reported in this paper.

## References

- S.-Y. Lee, S.-J. Park, TiO<sub>2</sub> photocatalyst for water treatment applications. *J. Ind. Eng. Chem.* **19**, 1761–1769 (2013)
- U. Thi Dieu Thuy, N. Quang Liem, C.M.A. Parlett, G. Lalev, K. Wilson, Synthesis of CuS and CuS/ZnS core/shell nanocrystals for photocatalytic degradation of dyes under visible light. *Catal. Commun.* **44**, 62–67 (2014)
- P. Soloman, C. Basha, V. Manickam, V. Ramamurthi, K. Koteeswaran, B. Subramanian, Electrochemical degradation of remazol black B dye effluent. *Clean: Soil, Air, Water* **37**, 889–900 (2009)
- T. Robinson, G. McMullan, R. Marchant, P. Nigam, Remediation of dyes in textile effluent: a critical review on current treatment technologies with a proposed alternative. *Biores. Technol.* **77**(3), 247–255 (2001)
- M. Rauf, S.S. Ashraf, Fundamental principles and application of heterogeneous photocatalytic degradation of dyes in solution. *Chem. Eng. J.* **151**(1–3), 10–18 (2009)
- M. Haroun, A. Idris, Treatment of textile wastewater with an anaerobic fluidized bed reactor. *Issue 1 Water Resour. Manag. New Approaches Technol.* **237**(1), 357–366 (2009)
- A. Malathi, V. Vasanthakumar, P. Arunachalam, J. Madhavan, M.A. Ghanem, A low cost additive-free facile synthesis of BiFeWO<sub>6</sub>/BiVO<sub>4</sub> nanocomposite with enhanced visible-light induced photocatalytic activity. *J. Colloid Interface Sci.* **506**, 553–563 (2017)
- Y. Xia, Q. Li, X. Wu, K. Lv, D. Tang, M. Li, Facile synthesis of CNTs/CaIn<sub>2</sub>S<sub>4</sub> composites with enhanced visible-light photocatalytic performance. *Appl. Surf. Sci.* **391**, 565–571 (2017)
- T. Hisatomi, J. Kubota, K. Domen, Recent advances in semiconductors for photocatalytic and photoelectrochemical water splitting. *Chem. Soc. Rev.* **43**(22), 7520–7535 (2014)
- J. Liu, D. Su, K. Wu, J.-P. Wang, High-moment magnetic nanoparticles. *J. Nanopart. Res.* **22**(3), 1–16 (2020)
- T.A. Rocha-Santos, Sensors and biosensors based on magnetic nanoparticles. *TrAC Trends Anal. Chem.* **62**, 28–36 (2014)
- A. Tomitaka, H. Arami, A. Ahmadivand, N. Pala, A.J. McGoron, Y. Takemura, M. Febo, M. Nair, Magneto-plasmonic nanostars for image-guided and NIR-triggered drug delivery. *Sci. Rep.* **10**(1), 1–10 (2020)
- A. Ahmadivand, B. Gerislioglu, P. Manickam, A. Kaushik, S. Bhansali, M. Nair, N. Pala, Rapid detection of infectious envelope proteins by magnetoplasmonic toroidal metasensors. *ACS Sens.* **2**(9), 1359–1368 (2017)
- C. Santhosh, V. Velmurugan, G. Jacob, S.K. Jeong, A.N. Grace, A. Bhatnagar, Role of nanomaterials in water treatment applications: a review. *Chem. Eng. J.* **306**, 1116–1137 (2016)
- R. Sathesh, K. Vignesh, A. Suganthi, M. Rajarajan, Visible light responsive photocatalytic applications of transition metal (M= Cu, Ni and Co) doped  $\alpha$ -Fe<sub>2</sub>O<sub>3</sub> nanoparticles. *J. Environ. Chem. Eng.* **2**(4), 1956–1968 (2014)
- Y. Yan, H. Guan, S. Liu, R. Jiang, Ag<sub>3</sub>PO<sub>4</sub>/Fe<sub>2</sub>O<sub>3</sub> composite photocatalysts with an n–n heterojunction semiconductor structure under visible-light irradiation. *Ceram. Int.* **40**, 9095–9100 (2014)
- T. Rocha, E. Nascimento, A. Silva, H. Oliveira, E. Garcia, L. Oliveira, D. Monteiro, M. Rodriguez, M. Pereira, Enhanced photocatalytic hydrogen generation from water by Ni(OH)<sub>2</sub> loaded on Ni-doped  $\delta$ -FeOOH nanoparticles obtained by one-step synthesis. *RSC Adv.* **3**, 20308 (2013)
- J. Theerthagiri, R.A. Senthil, A. Priya, J. Madhavan, R.J.V. Michael, M. Ashokkumar, Photocatalytic and photoelectrochemical studies of visible-light active  $\alpha$ -Fe<sub>2</sub>O<sub>3</sub>-g-C<sub>3</sub>N<sub>4</sub> nanocomposites. *RSC Adv.* **4**(72), 38222–38229 (2014)
- D.E. Fouad, C. Zhang, H. El-Didamony, L. Yingnan, T.D. Mekuria, A.H. Shah, Improved size, morphology and crystallinity of hematite ( $\alpha$ -Fe<sub>2</sub>O<sub>3</sub>) nanoparticles synthesized via the precipitation route using ferric sulfate precursor. *Results Phys.* **12**, 1253–1261 (2019)
- L. Zhang, Z. Wu, L. Chen, L. Zhang, X. Li, H. Xu, H. Wang, G. Zhu, Preparation of magnetic Fe<sub>3</sub>O<sub>4</sub>/TiO<sub>2</sub>/Ag composite microspheres with enhanced photocatalytic activity. *Solid State Sci.* **52**, 42–48 (2016)
- J. Kang, Q. Kuang, Z.-X. Xie, L.-S. Zheng, Fabrication of the SnO<sub>2</sub>/ $\alpha$ -Fe<sub>2</sub>O<sub>3</sub> hierarchical heterostructure and its enhanced photocatalytic property. *J. Phys. Chem. C* **115**(16), 7874–7879 (2011)
- T. Zhu, W. Li Ong, L. Zhu, G. Wei Ho, TiO<sub>2</sub> fibers supported  $\beta$ -FeOOH nanostructures as efficient visible light photocatalyst and room temperature sensor. *Sci. Rep.* **5**(1), 10601 (2015)
- F. Mughal, M. Muhyuddin, M. Rashid, T. Ahmed, M.A. Akram, M.A. Basit, Multiple energy applications of quantum-dot sensitized TiO<sub>2</sub>/PbS/CdS and TiO<sub>2</sub>/CdS/PbS hierarchical nanocomposites synthesized via p-SILAR technique. *Chem. Phys. Lett.* **717**, 69–76 (2019)
- F.U. Hassan, U. Ahmed, M. Muhyuddin, M. Yasir, M.N. Ashiq, M.A. Basit, Tactical modification of pseudo-SILAR process for enhanced quantum-dot deposition on TiO<sub>2</sub> and ZnO nanoparticles for solar energy applications. *Mater. Res. Bull.* **120**, 110588 (2019)
- S.S. Rao, I.K. Durga, C.V. Tulasi-Varma, D. Punnoose, S.-K. Kim, H.-J. Kim, Enhance the performance of quantum dot-sensitized solar cell by manganese-doped ZnS films as a passivation layer. *Org. Electron.* **26**, 200–207 (2015)
- M. Khan, M.H. Irfan, M. Israr, N. Rehman, T.J. Park, M.A. Basit, Comparative investigation of ZnO morphologies for optimal CdS quantum-dot deposition via pseudo-SILAR method. *Chem. Phys. Lett.* **744**, 137223 (2020)
- T.F. Khan, M. Muhyuddin, S.W. Husain, M.A. Basit, Synthesis and characterization of ZnO-ZnS nanoflowers for enhanced photocatalytic performance: ZnS decorated ZnO nanoflowers. In: *IEEE*; 2019. p. 60–65.
- S.J. Little, S.F. Ralph, N. Mano, J. Chen, G.G. Wallace, A novel enzymatic bioelectrode system combining a redox hydrogel with a carbon NanoWeb. *Chem. Commun.* **47**(31), 8886–8888 (2011)
- S. Zarezaeh, A. Habibi-Yangjeh, M. Mousavi, BiOBr and AgBr co-modified ZnO photocatalyst: a novel nanocomposite with pnn heterojunctions for highly effective photocatalytic removal of organic contaminants. *J. Photochem. Photobiol. A* **379**, 11–23 (2019)
- Z. Jing, S. Wu, Preparation and magnetic properties of spherical  $\alpha$ -Fe<sub>2</sub>O<sub>3</sub> nanoparticles via a non-aqueous medium. *Mater. Chem. Phys.* **92**(2–3), 600–603 (2005)
- A. Malathi, P. Arunachalam, J. Madhavan, A.M. Al-Mayouf, M.A. Ghanem, Rod-on-flake  $\alpha$ -FeOOH/BiOI nanocomposite: facile synthesis, characterization and enhanced photocatalytic performance. *Colloids Surf. A* **537**, 435–445 (2018)
- M.A. Basit, M.A. Abbas, E.S. Jung, J.H. Bang, T.J. Park, Improved light absorbance and quantum-dot loading by macroporous TiO<sub>2</sub> photoanode for PbS quantum-dot-sensitized solar cells. *Mater. Chem. Phys.* **196**, 170–176 (2017)
- B. Wang, Q. Wei, S. Qu, Synthesis and characterization of uniform and crystalline magnetite nanoparticles via oxidation-precipitation

- and modified co-precipitation methods. *Int. J. Electrochem. Sci.* **8**(3), 3786–3793 (2013)
34. Y.J. Zhang, L.C. Liu, L.L. Ni, B.L. Wang, A facile and low-cost synthesis of granulated blast furnace slag-based cementitious material coupled with  $\text{Fe}_2\text{O}_3$  catalyst for treatment of dye wastewater. *Appl. Catal. B* **138**, 9–16 (2013)
35. Y. Liu, X. Liu, Y. Zhao, D.D. Dionysiou, Aligned  $\alpha$ -FeOOH nanorods anchored on a graphene oxide-carbon nanotubes aerogel can serve as an effective Fenton-like oxidation catalyst. *Appl. Catal. B* **213**, 74–86 (2017)
36. F. Wang, X. Qin, Y. Meng, Z. Guo, L. Yang, Y. Ming, Hydrothermal synthesis and characterization of  $\alpha$ - $\text{Fe}_2\text{O}_3$  nanoparticles. *Mater. Sci. Semicond. Process.* **16**(3), 802–806 (2013)
37. T. Fan, D. Pan, H. Zhang, Study on formation mechanism by monitoring the morphology and structure evolution of nearly monodispersed  $\text{Fe}_3\text{O}_4$  submicroparticles with controlled particle sizes. *Ind. Eng. Chem. Res.* **50**(15), 9009–9018 (2011)
38. B.R. Devi, R. Raveendran, A. Vaidyan, Synthesis and characterization of  $\text{Mn}^{2+}$ -doped ZnS nanoparticles. *Pramana* **68**(4), 679–687 (2007)
39. H. Yin, Y. Wada, T. Kitamura, S. Yanagida, Photoreductive dehalogenation of halogenated benzene derivatives using ZnS or CdS nanocrystallites as photocatalysts. *Environ. Sci. Technol.* **35**(1), 227–231 (2001)
40. U. Gangopadhyay, K. Kim, D. Mangalaraj, J. Yi, Low cost CBD ZnS antireflection coating on large area commercial mono-crystalline silicon solar cells. *Appl. Surf. Sci.* **230**(1–4), 364–370 (2004)
41. A. Amani-Ghadim, S. Alizadeh, F. Khodam, Z. Rezvani, Synthesis of rod-like  $\alpha$ -FeOOH nanoparticles and its photocatalytic activity in degradation of an azo dye: Empirical kinetic model development. *J. Mol. Catal. A Chem.* **408**, 60–68 (2015)
42. R. Rahimi, M. Rabbani, G. Kareh, Comparative study of photocatalytic activity for three type  $\text{Fe}_3\text{O}_4$  prepared in presence of different hydrolysis agent. In: *The 19th International Electronic Conference on Synthetic Organic Chemistry: 2015: Multidisciplinary*. Digital Publishing Institute; 2015.
43. A.J. Deotale, R. Nandedkar, Correlation between particle size, strain and band gap of iron oxide nanoparticles. *Mater. Today Proc.* **3**(6), 2069–2076 (2016)
44. G. Saini, S. Kaur, S. Tripathi, C. Mahajan, H. Thanga, A. Verma, Spectroscopic studies of rhodamine 6G dispersed in polymethylcyanoacrylate. *Spectrochim. Acta Part A Mol. Biomol. Spectrosc.* **61**(4), 653–658 (2005)
45. I. Ali, M. Muhyuddin, N. Mullani, D.W. Kim, D.H. Kim, M.A. Basit, T.J. Park, Modernized  $\text{H}_2\text{S}$ -treatment of  $\text{TiO}_2$  nanoparticles: Improving quantum-dot deposition for enhanced photocatalytic performance. *Curr. Appl. Phys.* **20**(3), 384–390 (2020)
46. Y. Shi, H. Li, L. Wang, W. Shen, H. Chen, Novel  $\alpha$ - $\text{Fe}_2\text{O}_3$ /CdS cornlike nanorods with enhanced photocatalytic performance. *ACS Appl. Mater. Interfaces* **4**(9), 4800–4806 (2012)
47. P.K. Boruah, S. Szunerits, R. Boukherroub, M.R. Das, Magnetic  $\text{Fe}_3\text{O}_4@ \text{V}_2\text{O}_5/\text{rGO}$  nanocomposite as a recyclable photocatalyst for dye molecules degradation under direct sunlight irradiation. *Chemosphere* **191**, 503–513 (2018)
48. V.J. Babu, S. Vempati, T. Uyar, S. Ramakrishna, Review of one-dimensional and two-dimensional nanostructured materials for hydrogen generation. *Phys. Chem. Chem. Phys.* **17**(5), 2960–2986 (2015)
49. R.T. da Silva, E.S. Nascimento, A.C. da Silva, O.H. dos Santos, E.M. Garcia, L.C.A. de Oliveira, D.S. Monteiro, M. Rodriguez, M.C. Pereira, Enhanced photocatalytic hydrogen generation from water by  $\text{Ni}(\text{OH})_2$  loaded on Ni-doped  $\delta$ -FeOOH nanoparticles obtained by one-step synthesis. *RSC Adv.* **3**(43), 20308–20314 (2013)
50. S. Balu, K. Uma, G.-T. Pan, T.C.-K. Yang, S.K. Ramaraj, Degradation of methylene blue dye in the presence of visible light using  $\text{SiO}_2@ \alpha$ - $\text{Fe}_2\text{O}_3$  nanocomposites deposited on  $\text{SnSn}_2$  flowers. *Materials* **11**(6), 1030 (2018)
51. H.M. Naeem, M. Muhyuddin, R. Rasheed, A. Noor, M.A. Akram, M.N. Aashiq, M.A. Basit, Simplistic wet-chemical coalescence of ZnO with  $\text{Al}_2\text{O}_3$  and  $\text{SnO}_2$  for enhanced photocatalytic and electrochemical performance. *J. Mater. Sci.: Mater. Electron.* **30**(15), 14508–14518 (2019)
52. M. Muhyuddin, T.F. Khan, M.A. Akram, I. Ali, T.J. Park, M.A. Basit, Significantly improved photo-and electro-chemical performance of CuS. PbS nanocomposites for dye degradation and paintable counter electrodes. *J. Photochem. Photobiol. A Chem.* **400**, 112720 (2020)

**Publisher's Note** Springer Nature remains neutral with regard to jurisdictional claims in published maps and institutional affiliations.